無容器法により作製した LaGaO₃ ガラスの構造，振動特性および電子状態の解析

吉本幸平，増野敦信，佐藤　至，江面嘉信，井上博之，上田　基，水口雅史，山本優也

Structural, Vibrational, and Electronic Analysis of LaGaO₃ Glass Prepared through Containerless Processing

Kohei YOSHIMOTO, Atsunobu MASUNO, Itaru SATO, Yoshinobu EZURA, Hiroyuki INOUE, Motoi UEDA, Masafumi MIZUGUCHI and Yuya YAMAMOTO

　無容器法は，融液－容器界面で生じる不均一核生成を抑制することにより，融液のガラス形成を大きく促進することができる．近年，筆者らはこの手法を用いて，通常のるつぼ熔解では得られない LaGaO₃ ガラスの合成に成功した．LaGaO₃ ガラスは，高い屈折率や紫外～赤外域における広い光透過性など，典型的な網目形成酸化物を主体とするガラスとは異なる光学特性を有しており，新しい光機能材料としての応用が期待される．本研究では，LaGaO₃ ガラスにおける特異な光学特性の構造的起源を明らかにするため，ガラスの局所構，振動特性，電子状態の解析を行った．実験的に取得した回折データと分子動力学計算から LaGaO₃ ガラスの構造モデルを構築し，振動スペクトル計算や電子状態解析によって，ガラスの局所構造が振動特性や電子状態へ及ぼす影響について考察した．本研究で得られた知見は，無容器法を用いた新規光機能ガラスの組成設計に活用できるものと期待される．

　Containerless processing is useful for vitrifying compositions with low glass-forming ability because it suppresses heterogeneous nucleation from the container wall. Using this method, we recently synthesized LaGaO₃ glass, which cannot be obtained using an ordinal melt-quenching process. LaGaO₃ glass exhibited excellent optical properties such as a high refractive index and wide optical transparency from the ultraviolet to infrared range, which are unusual in a typical oxide glass containing network-formers, and can be a new optical functional material for various applications. In this study, we investigated the local structures, vibrational characteristics, and electronic properties of LaGaO₃ glass to reveal the structural origins of unique optical properties. A structural model of LaGaO₃ glass was constructed from diffraction data and molecular dynamics simulations. In addition, the vibrational density of states and *ab initio* calculations were applied to evaluate the vibrational characteristics and electronic structures of LaGaO₃ glass.

1 Introduction

　Ga₂O₃-based systems occasionally form glass even without the presence of network-former (NWF) oxides such as SiO₂, B₂O₃, and P₂O₅. Such unconventional gallate glasses have attracted interest owing to their superior optical properties, including long infrared cut-off wavelengths, high refractive indices, and large nonlinear optical properties [1], [2]. However, NWF-free systems generally show low glass-forming abilities, making it difficult to obtain bulk glass. Containerless processing is suitable for obtaining bulk glass with such unconventional NWF-free compositions because it suppresses heterogeneous nucleation and promotes a deep undercooling of the melt [3]–[5]. In recent years, we reported the vitrification of a LaGaO₃ composition using containerless processing [6]. Owing to its high oxygen polarizability and low maximum phonon energy, LaGaO₃ glass exhibits excellent optical properties, such as a high refractive index (1.954), relatively low dispersion (33.6 in Abbe number), wide optical transmittance range (280 nm to 8 μm), and efficient fluorescence emission by rare-earth activation [6], [7]. These results indicate the significant advantage of rare-earth-gallate glasses for various optical applications such as lenses, lasers, and infrared optics. Nevertheless, the local atomic and electronic structures, which are the physical origins of the optical properties, have not been investigated well in rare-earth-gallate glasses.

　In this study, we evaluated three important aspects of

LaGaO$_3$ glass: local atomic structures, vibrational characteristics, and electronic structures. To achieve this, high-energy X-ray and neutron diffraction experiments, classical molecular dynamics (CMD), and *ab initio* molecular dynamics (AIMD) simulations were conducted. We constructed a detailed structural model of LaGaO$_3$ glass and investigated the origins of unique vibrational and optical properties by computing vibrational spectra and *ab initio* electronic structure calculations.

2 Experimental and Computational Details

2.1. Glass Synthesis

High-purity La$_2$O$_3$ (5N) and Ga$_2$O$_3$ (4N) powders were mixed in a stoichiometric ratio of LaGaO$_3$. The mixture was pressed into pellets and sintered at 1473 K for 12 h under ambient atmosphere. Using an aerodynamic levitation furnace, the pellets were placed on a conical nozzle, levitated by an O$_2$ gas flow, and melted using a CO$_2$ laser (Fig. 1). After melting for several tens of seconds, the CO$_2$ laser was turned off and the sample was cooled at a rate of several hundreds of kelvins per second, forming spherical glass with a diameter of 2–3 mm. The glass was annealed near the glass transition temperature (1026 K [6]) for 10 min to remove the internal strain.
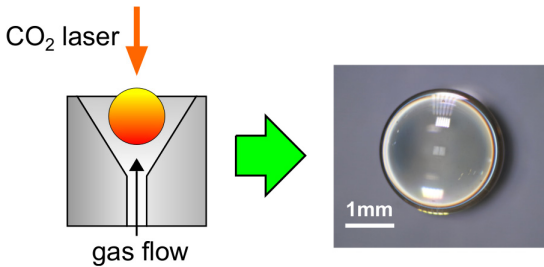

Fig. 1 Schematic illustration of glass synthesis using the aerodynamic levitation technique, and a photograph of LaGaO$_3$ glass.

2.2. Diffraction Experiments

High-energy X-ray and neutron diffraction experiments were conducted at the BL04B2 beamline of the SPring-8 synchrotron radiation facility [8] and at the high-intensity total diffractometer NOVA installed at BL21 of the Materials and Life Science Experimental Facility at the J-PARC spallation neutron source [9], respectively. The energy of X-ray was 113 keV and the wavelength range of the incident neutron beam was $0.12 < \lambda < 8.3$ Å. The observed scattering intensities for the samples were corrected for polarization, absorption, background, multiple, and incoherent scattering,

and normalized based on the incident beam profile. The total correlation functions, $T(r)$s, were then obtained through a Fourier transformation of the structure factors with a Lorch modification function [10]. The scattering vector from 0.3 to 25 Å^{-1} for the X-ray and 0.5 to 35 Å^{-1} for the neutron beam was used for the Fourier transformation.

2.3. Classical Molecular Dynamics Simulation

CMD simulations were conducted using the LAMMPS code [11]. We used sets of interatomic potential parameters determined in our previous study [12]. Coulombic interactions were calculated using the Ewald summation method with a relative precision of 10^{-6}. The structural model of the LaGaO$_3$ glass contained 2500 atoms. The size of the cubic cells was set to reproduce the experimental density (5.91 g/cm^3 [6]) and periodic boundary conditions were applied. The initial atomic configuration was randomly generated with constraints between the atom pairs to avoid overlapping atoms. The simulation was executed at a time step of 1 fs, and an *NVT* (canonical) ensemble with a Nose-Hoover thermostat was applied. The model was first equilibrated at 5000 K for 50 ps and then melted at 3000 K for 50 ps. The melt was cooled to 300 K at a nominal cooling rate of 10 K/ps and equilibrated at 300 K for another 50 ps.

2.4. Vibrational Analysis

The vibrational density of states (VDOS) was computed from the CMD structural model based on a harmonic approximation [13], [14]. The dynamical matrix, *i.e.*, the matrix of the second derivatives of the total energy with respect to the Cartesian coordinates, was computed through a numerical evaluation of the first derivatives obtained from the minute atomic displacement. The mass-weighted dynamical matrix was diagonalized to obtain eigenvalues ω_j^2, where ω_j is the eigenfrequency at mode j and eigenvectors $\mathbf{e}^j$. The total VDOS, $g(\omega)$, is obtained as

$$g(\omega) = \frac{1}{3N} \sum_{j=1}^{3N} \delta(\omega - \omega_j),$$

where N is the number of atoms in the cell, and δ is convoluted by a Gaussian function with a full width at half-maximum of 15 cm^{-1}. A partial VDOS, $g_\alpha(\omega)$, is defined by

$$g_a(\omega) = \frac{1}{3N} \sum_{j=1}^{3N} \sum_{i \in \alpha} w_\alpha^j \delta(\omega - \omega_j),$$

where w_α^j is a weight factor, and α represents the type of atom or part of the structure. For the partial VDOS of an atom α, the weight factor is defined as $w_\alpha^j = \left| \mathbf{e}_i^j \right|^2$. To investigate the atomic motion for different eigenmodes, the eigenvectors were projected onto several vibrational modes of

typical structural units. For instance, the weight factor of the stretching mode of the Ga–O bond, $w^j_{\text{Ga-O,s}}$, is given as

$$w^j_{\text{Ga-O,s}} = \frac{\sum_i \left| \tilde{\mathbf{u}}^j_i \cdot \frac{\mathbf{r}_{\text{Ga-O}}}{|\mathbf{r}_{\text{Ga-O}}|} \right|^2}{\sum_i \left| \tilde{\mathbf{u}}^j_i \right|^2},$$

where $\mathbf{r}_{\text{Ga-O}}$ is the Ga–O bond vector and $\tilde{\mathbf{u}}^j_i = \mathbf{u}^j_i - \mathbf{u}^j_{\text{Ga}}$ is the displacement of the O atom i relative to the displacement of its Ga neighbor. In addition, $\mathbf{u}^j_i$ is the Cartesian displacement vector, which is obtained as $\mathbf{u}^j_i = \mathbf{e}^j_i / m_i^{1/2}$, where m_i is the mass of the atom. By replacing $\mathbf{r}_{\text{Ga-O}}$ with a specific vector, it is possible to calculate other vibration modes and structural units [12]. For the vibrational analysis above, a structural model containing 750 atoms was prepared. To prevent the occurrence of imaginary frequencies, the dynamical matrix was computed after further cooling the structural model from 300 K to below 1.0×10^{-5} K under the *NVT* ensemble to minimize the internal energy of the system.

2.5. *Ab Initio* Calculation

Ab initio calculations based on density functional theory (DFT) were conducted using a hybrid Gaussian and plane wave method as implemented in the CP2K code [15]. For each atom, we used molecularly optimized short-range double-zeta basis sets [16]. The cutoff of the plane wave basis set for the electron density was set to 500 Ry. The generalized gradient approximation (GGA) was adopted to treat exchange-correlation effects in the form of the Perdew–Burke–Ernzerhof energy functional [17]. Goedecker–Teter–Hutter norm-conserving pseudopotentials [18] were used with the following valence configurations: La $(5s^25p^65d^16s^2)$, Ga $(3d^{10}4s^24p^1)$, and O $(2s^22p^4)$. Periodic boundary conditions were applied with a single Γ point in the Brillouin zone. A Born-Oppenheimer AIMD simulation was conducted at a time step of 2 fs, and an *NVT* ensemble with a Nose-Hoover thermostat was applied. The initial atomic configuration was created through the CMD simulation of 100 atoms in a cubic cell, which reproduced the experimental density. The structural model of LaGaO₃ glass was obtained by holding the initial atomic configuration at 2400 K for 10 ps, lowering the temperature to 300 K at a nominal cooling rate of 100 K/ps, and equilibration at 300 K for 10 ps.

3 Results and Discussion

3.1. Local Structures of LaGaO₃ Glass

Fig. 2 shows the total correlation functions of LaGaO₃

glass. The correlation peaks appearing at approximately 1.8 and 2.5 Å correspond to the Ga–O and La–O bonds, respectively, revealing that the average bond lengths of Ga–O and La–O in LaGaO₃ glass are 1.84 and 2.46 Å, respectively. The CMD model reproduces the experimental results well in the first nearest-neighbor correlations of Ga–O and La–O, whereas in the AIMD, the peak position of the Ga–O bond is located slightly on the long-distance side. By contrast, at 3–5 Å, the results of AIMD are more consistent with the experimental results in comparison with the CMD, suggesting that the AIMD can better reproduce the correlations of the second nearest-neighbor, such as O–O and cation–cation.
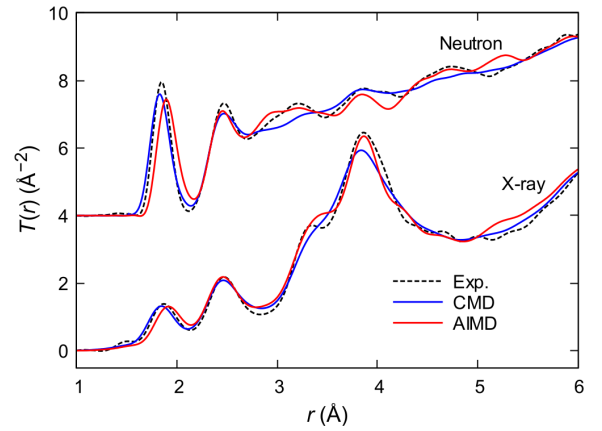

Fig. 2 Experimental and simulated total correlation functions of LaGaO₃ glass.

In addition, Fig. 3 shows the coordination number distribution of LaGaO₃ glass and the connectivity between the cation-oxygen polyhedra. It was confirmed that the Ga atoms formed a 4–6 coordination with O. The average coordination numbers of Ga–O and $N_{\text{Ga-O}}$ in the CMD and AIMD show similar values of 4.3 and 4.4, respectively. By contrast, the average coordination number of La–O, *i.e.*, $N_{\text{La-O}}$, is 7.4 and 7.8 in CMD and AIMD, respectively, the latter of which shows a larger value. From Fig. 3(e), it can be seen that the coordination number of O–Ga, $N_{\text{O-Ga}}$, is 0–3. That is, in LaGaO₃ glass, there are four types of oxygen depending on the coordination environment: free oxygen, O_f ($N_{\text{O-Ga}} = 0$); non-bridging oxygen, O_{nb} ($N_{\text{O-Ga}} = 1$); bridging oxygen, O_b ($N_{\text{O-Ga}} = 2$); and tricluster oxygen, O_t ($N_{\text{O-Ga}} = 3$). The average coordination numbers of O–La, *i.e.*, $N_{\text{La-O}}$, in O_f, O_{nb}, O_b, and O_t were 3.9, 2.8, 1.8, and 1.0 for CMD and 4.0, 2.9, 2.2, and 1.2 for AIMD, respectively. This means that each oxygen atom coordinates with approximately four cations on average, regardless of the $N_{\text{O-Ga}}$ value.

Regarding the cation–oxygen polyhedral connectivity, the fractions of corner-sharing GaO_x–GaO_x and those of edge-
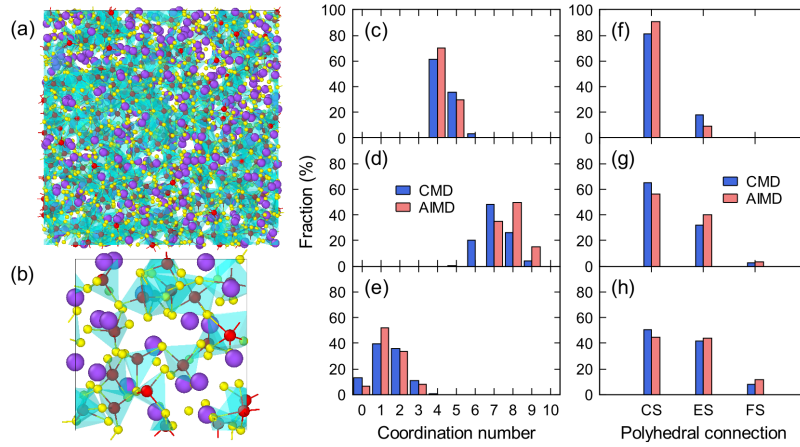
Fig. 3　Structural models for LaGaO₃ glass obtained through (a) CMD and (b) AIMD simulations. La, Ga, and O atoms are colored purple, red, and yellow, respectively. The coordination number distribution of (c) O around Ga, (d) O around La, and (e) Ga around O for the structural models of LaGaO₃ glass. The polyhedral connections of (f) GaO$_x$–GaO$_x$, (g) GaO$_x$–LaO$_y$, and (h) LaO$_y$–LaO$_y$ linkages for the structural models of LaGaO₃ glass. CS, ES, and FS represent corner-, edge-, and face-sharing of oxygen, respectively.

and face-sharing GaO$_x$–LaO$_y$ and LaO$_y$–LaO$_y$ are slightly higher in AIMD than in CMD. The AIMD results show that the majority of GaO$_x$–GaO$_x$ linkages form corner sharing, whereas approximately 10% form edge-sharing. Moreover, for the GaO$_x$–LaO$_y$ and LaO$_y$–LaO$_y$ linkages, the fractions of edge- and face-sharing connectivity were even higher. Some structural features confirmed in LaGaO₃ glass, such as edge-sharing cation–oxygen polyhedral linkages and oxygen tri-clusters, are unusual in NWF oxides such as SiO₂, B₂O₃, and P₂O₅, and are unique to glass systems that do not contain NWF oxides [14], [19], [20].

3.2. Correlation between Glass Structures and Vibration Characteristics

Fig. 4 shows the Raman scattering spectra [6] and calculated VDOS. The Raman scattering spectra showed distinct peaks at 300, 530, and 650 cm^{-1}. However, VDOS showed peaks at 100 and 600 cm^{-1} and a broad shoulder at 700–850 cm^{-1}. It is not always possible to compare the spectral shape of the total VDOS and the Raman spectra because the cross-section of Raman scattering differs depending on the structural units and modes. To compare the peak intensity and peak position of VDOS with Raman spectroscopy, it is necessary to evaluate the partial VDOS corresponding to certain structural units and modes. Fig. 4(b) also displays the partial VDOS of the La, Ga, and O atoms. The vibrational spectrum of the La atoms was symmetric and located at 100 cm^{-1}. The vibration of the Ga atoms has a broad peak at 180 cm^{-1} and a slight shoulder at approximately 630 cm^{-1}. The O atoms showed a large contribution within the entire range. These results indicate that the high-frequency range (above 400 cm^{-1}) is dominated by the vibration of O bonded with Ga.
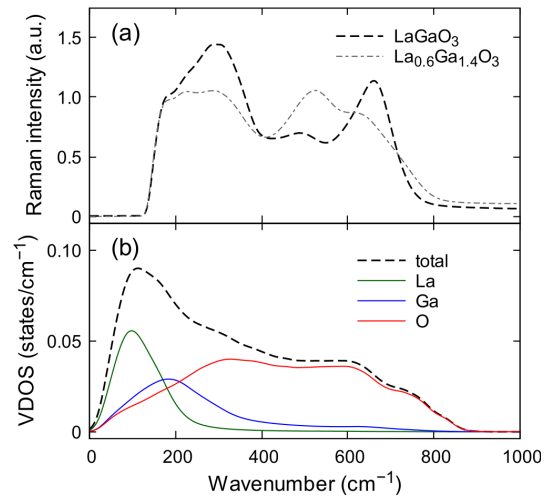

Fig. 4　(a) The Raman scattering spectra of LaGaO₃ and La₀.₆Ga₁.₄O₃ glasses [6]. The Raman spectra at below 180 cm^{-1} was cut off by a filter to remove Rayleigh scattering. (b) The calculated total VDOS and the partial VDOS of La, Ga, and O atoms for LaGaO₃ glass.

As shown in Fig. 5, the vibrational spectrum of the O atoms was further deconvoluted into the contributions of O$_f$, O$_{nb}$, O$_b$, and O$_t$. In addition, O$_f$ shows a nearly symmetrical peak at 320 cm^{-1}. Because O$_f$ corresponds to the oxygen atoms coordinated only with La, it is suggested that the peak at near 300 cm^{-1} within the Raman spectrum is caused by the vibration of the La–O bonds. It has also been reported that in La₂O₃-containing glass, a Raman signal at approximately 300 cm^{-1} was assigned to the stretching mode of the La–O bonds [21], supporting the results of this study.
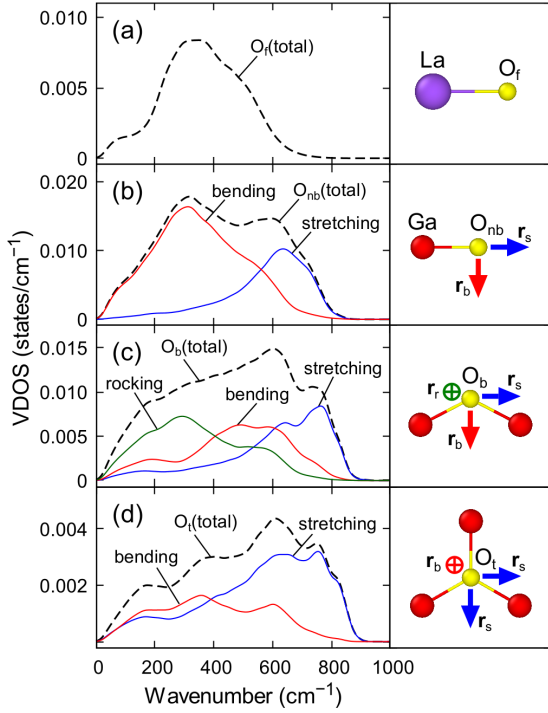
Fig. 5 Partial VDOS of LaGaO$_3$ glass for the projections onto the vibrations of (a) O$_f$, (b) O$_{nb}$, (c) O$_b$, and (d) O$_t$. The structural units and atomic displacements are schematically shown on the right side of the Figure. In addition, **r**$_s$, **r**$_b$, and **r**$_r$ denote the displacement vectors representing the stretching, bending, and rocking modes, respectively.

According to a previous study conducted by Fukumi *et al.*, the Raman peak at 530 cm^{-1} was assigned to the Ga–O–Ga bending mode, and the peak at 650 cm^{-1} was assigned to the stretching vibration of GaO$_x$ polyhedra, including non-bridging oxygen [22]. In the VDOS, the bending mode of the Ga–O$_b$–Ga linkage shows a large contribution to the region at 500 cm^{-1}, which is consistent with the assignment at 530 cm^{-1} by Fukumi *et al.* From Fig. 5, the stretching modes of the Ga–O$_{nb}$ bonds and Ga–O$_b$–Ga linkages show a large contribution at 650 cm^{-1}, which supports the claim that the component at 650 cm^{-1} within the Raman spectra is attributed to the vibration of GaO$_x$ polyhedra, including non-bridging oxygen.

In LaGaO$_3$ glass, the fraction at approximately 750 cm^{-1} within the Raman spectrum is weak, whereas in La$_{0.6}$Ga$_{1.4}$O$_3$ glass with a larger Ga$_2$O$_3$ content, a broad shoulder peak appears within this high-frequency region (Fig. 4). This high-frequency component was not assigned in the previous study by Fukumi *et al.* [22], and its structural origin is unknown. From the results of VDOS, the contribution of the stretching modes of Ga–O$_b$–Ga linkages and Ga$_3$–O$_t$ tri-clusters are dominant at approximately 750 cm^{-1}, indicating that this high-frequency component originates from the bridging and tri-cluster oxygens. Because the vibration mode at 750 cm^{-1} is

at the highest frequency in the La$_2$O$_3$–Ga$_2$O$_3$ glass system, it is strongly expected that the influence on the optical properties in the infrared region will be significant. We previously reported that the infrared absorption edge of La$_2$O$_3$–Ga$_2$O$_3$ glass shifted to a longer wavelength as the La$_2$O$_3$ content increased [6]. It is considered that this compositional dependence of the infrared absorption edge is due to the decrease in the bridging and tri-cluster oxygen with increasing La$_2$O$_3$ content, which results in a decrease in the vibrational component at 750 cm^{-1}.

3.3. Analysis of Electronic Structures

Fig. 6 shows the projected electronic density of states (DOS) of LaGaO$_3$ glass derived from the AIMD structural model. The simulated band gap energy of LaGaO$_3$ glass was 3.3 eV, which is smaller than the experimental value of 4.4 eV [6]. This is because of the well-known trend in which DFT with GGA inherently underestimates the band gap. Despite this limitation, DFT calculations are still useful for analyzing the band structures. The band between -19 and -12 eV is composed of La5p, Ga3d, and O2s orbitals, whereas the upper valence band between -7 eV and the Fermi level (0 eV) is dominated by the O2p orbital. In the upper valence band, the contribution of La and Ga by hybridization with the O2p orbital is weak, indicating the high ionic nature of oxygen. Further deconvolution of the electronic DOS into each type of oxygen atom (O$_f$, O$_{nb}$, O$_b$, and O$_t$) reveals that the top of the valence band is composed of O$_f$ and O$_{nb}$. In addition, our simulation results suggest that the lower part of the conduction band is mainly composed of La5d and La4f orbitals.

We also determined the effective charge of each atom in LaGaO$_3$ glass using the Bader method [23]. The effective charges of La, Ga, and O atoms were derived as $+2.08e$, $+1.76e$, and $-1.28e$, respectively, which also supports the high ionicity of LaGaO$_3$ glass. The effective charges of O$_f$, O$_{nb}$, O$_b$, and O$_t$ were derived as $-1.30e$, $-1.28e$, $-1.27e$, and $-1.26e$, respectively, indicating that oxygen with smaller $N_{O–Ga}$ shows a higher effective charge. This is because La has a lower electronegativity than Ga (1.10 and 1.81 for La and Ga, respectively) [24], and the La–O bond is more ionic than the Ga–O bond and shows a greater electron donation to the oxygen. However, the difference in the effective charge between each type of oxygen was not significantly large; thus, the electron density may be delocalized throughout the oxygen atoms. The experimentally determined average oxygen polarizabilities of LaGaO$_3$ glass were 2.36 Å^3 [6], which is significantly larger than that of other

oxide glasses containing NWF oxides [25]. From the results of our DFT calculations, the unique characteristics such as a large oxygen polarizability and high refractive index of $LaGaO_3$ glass can be understood by the high electron charge density of oxygen, which is significantly enhanced by the high electron donating ability of La.
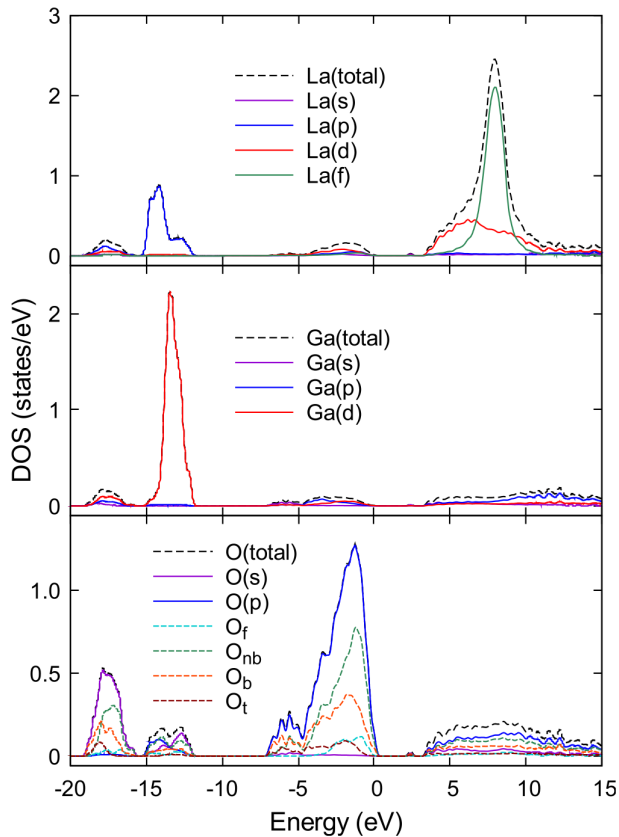

Fig. 6 The projected electronic DOS for $LaGaO_3$ glass.

4 Conclusion

We analyzed the local atomic structures, vibrational characteristics, and electronic structures of $LaGaO_3$ glasses prepared through a containerless processing. The structural models constructed by the diffraction experiments, CMD, and AIMD simulations revealed the average bond distances, average coordination numbers, and polyhedral connectivity of $LaGaO_3$ glass. Several unique structural features, such as oxygen tri-clusters and edge-sharing GaO_x–GaO_x polyhedral linkages, which are different from those of NWF oxides, were confirmed. The analysis of the calculated VDOS for $LaGaO_3$ glass showed good agreement with the assignments of the Raman spectrum. It was revealed that the broad component at the highest frequency (750 cm^{-1}) originated from the stretching vibrations of the bridging and tri-cluster oxygen, which explains the compositional dependence of the infrared absorption edge in the La_2O_3–Ga_2O_3 glass system.

The projected electronic DOS provides clear insight into the band structures of $LaGaO_3$ glass, *i.e.*, the upper part of the valence band is dominated by the O2p orbital, and the conduction band is mainly composed of La5d and La4f orbitals. A Bader charge analysis indicates that La, with its high electron-donating ability, significantly enhances the electron density of the outer valence of oxygen, resulting in a high oxygen polarizability and high refractive index of $LaGaO_3$ glass.

References

[1] W. H. Dumbaugh, "Heavy metal oxide glasses containing Bi_2O_3," *Phys. Chem. Glasses*, vol. 27, no. 3, pp. 119–123, 1986.

[2] S. Sakka, "Formation, structure, and properties of unconventional glasses containing gallium oxide," *Glass Phys. Chem.*, vol. 24, no. 3, pp. 257–267, 1998.

[3] J. Yu, Y. Arai, T. Masaki, T. Ishikawa, S. Yoda, S. Kohara, H. Taniguchi, M. Itoh, and Y. Kuroiwa, "Fabrication of $BaTi_2O_5$ glass-ceramics with unusual dielectric properties during crystallization," *Chem. Mater.*, vol. 18, no. 8, pp. 2169–2173, 2006.

[4] A. Masuno, H. Inoue, K. Yoshimoto, and Y. Watanabe, "Thermal and optical properties of La_2O_3–Nb_2O_5 high refractive index glasses," *Opt. Mater. Express*, vol. 4, no. 4, pp. 710–718, 2014.

[5] G. A. Rosales-Sosa, A. Masuno, Y. Higo, H. Inoue, Y. Yanaba, T. Mizoguchi, T. Umada, K. Okamura, K. Kato,

and Y. Watanabe, "High elastic moduli of a $54Al_2O_3$–$46Ta_2O_5$ glass fabricated via containerless processing," *Sci. Rep.*, vol. 5, no, 15233, 2015.

[6] K. Yoshimoto, A. Masuno, M. Ueda, H. Inoue, H. Yamamoto, and T. Kawashima, "Low phonon energies and wideband optical windows of La_2O_3–Ga_2O_3 glasses prepared using an aerodynamic levitation technique," *Sci. Rep.*, vol. 7, no. 45600, 2017.

[7] K. Yoshimoto, Y. Ezura, M. Ueda, A. Masuno, and H. Inoue, "2.7 μm mid-infrared emission in highly erbium-doped lanthanum gallate glasses prepared via an aerodynamic levitation technique," *Adv. Opt. Mater.*, vol. 6, no. 1701283, 2018.

[8] S. Kohara, M. Itou, K. Suzuya, Y. Inamura, Y. Sakurai, Y. Ohishi, and M. Takata, "Structural studies of disordered materials using high-energy X-ray diffraction from ambient to extreme conditions," *J. Phys.: Condens. Matter*, vol. 19, no. 506101, 2007.

[9] T. Otomo, K. Suzuya, M. Misawa, N. Kaneko, H. Ohshita, K. Ikeda, M. Tsubota, T. Seya, T. Fukunaga, K. Itoh, *et al.* "Fundamental research of hydrogen storage mechanism with high-intensity total diffractometer," *KENS Rep.* vol. 17, pp. 28–36, 2011.

[10] E. Lorch, "Neutron diffraction by germania, silica and radiation-damaged silica glasses," *J. Phys. C: Solid State Phys.*, vol. 2, no. 2, pp. 229–237, 1969.

[11] S. Plimpton, "Fast parallel algorithms for short-range molecular dynamics," *J. Comput. Phys.*, vol. 117, no. 1, pp. 1–19, 1995.

[12] K. Yoshimoto, A. Masuno, I. Sato, Y. Ezura, H. Inoue, M. Ueda, M. Mizuguchi, Y. Yanaba, T. Kawashima, T. Oya, *et al.* "Principal vibration modes of the La_2O_3–Ga_2O_3 binary glass originated from diverse coordination environments of oxygen atoms," vol. 124, no. 24, pp. 5056–5066, 2020.

[13] S. N. Taraskin and S. R. Elliott, "Nature of vibrational excitations in vitreous silica," *Phys. Rev. B*, vol. 56, no. 14, pp. 8605–8622, 1997.

[14] H. Inoue, A. Masuno, S. Kohara, and Y. Watanabe, "The local structure and vibrational properties of $BaTi_2O_5$ glass revealed by molecular dynamics simulation," *J. Phys. Chem. B*, vol. 117, no. 22, pp. 6823–6829, 2013.

[15] J. VandeVondele, M. Krack, F. Mohamed, M. Parrinello, T. Chassaing, and J. Hutter, "Quickstep: Fast and accurate density functional calculations using a mixed Gaussian and plane waves approach," *Comput. Phys. Commun.*, vol. 167, no. 2, pp. 103–128, 2005.

[16] J. VandeVondele and J. Hutter, "Gaussian basis sets for accurate calculations on molecular systems in gas and condensed phases," *J. Chem. Phys.*, vol. 127, no. 11, pp. 114105–114109, 2007.

[17] J. P. Perdew, K. Burke, and M. Ernzerhof, "Generalized gradient approximation made simple," *Phys. Rev. Lett.*, vol. 77, no. 18, pp. 3865–3868, 1996.

[18] S. Goedecker, M. Teter, and J. Hutter, "Separable dual-space Gaussian pseudopotentials," *Phys. Rev. B*, vol. 54, no. 3, pp. 1703–1710, 1996.

[19] J. Du, C. J. Benmore, R. Corrales, R. T. Hart, and J. K. R. Weber, "A molecular dynamics simulation interpretation of neutron and x-ray diffraction measurements on single phase Y_2O_3–Al_2O_3 glasses," *J. Phys.: Condens. Matter*, vol. 21, no. 205102, 2009.

[20] A. Masuno, S. Kohara, A. C. Hannon, E. Bychkov, and H. Inoue, "Drastic connectivity change in high refractive index lanthanum niobate glasses," *Chem. Mater.*, vol. 25, no. 15, pp. 3056–3061, 2013.

[21] L. G. Hwa, J. G. Shiau, and S. P. Szu, "Polarized Raman scattering in lanthanum gallogermanate glasses," *J. Non-Cryst. Solids*, vol. 249, no. 1, pp. 55–61, 1999.

[22] K. Fukumi and S. Sakka, "Raman spectra of binary alkali and alkaline earth gallate crystals and glasses," *Phys. Chem. Glasses*, vol. 29, no. 1, pp. 1–8, 1988.

[23] W. Tang, E. Sanville, and G. A. Henkelman, "A grid-based Bader analysis algorithm without lattice bias," *J. Phys.: Condens. Matter*, vol. 21, no. 084204, 2009.

[24] L. Pauling, "The nature of the chemical bond. IV. The energy of single bonds and the relative electronegativity of atoms," *J. Am. Chem. Soc.*, vol. 54, no. 9, pp. 3570–3582, 1932.

[25] V. Dimitrov and T. Komatsu, "Electronic polarizability, optical basicity and non-linear optical properties of oxide glasses," *J. Non-Cryst. Solids*, vol. 249, no. 2–3, pp. 160–179, 1999.

吉本幸平　Kohei YOSHIMOTO
研究開発本部　材料・要素技術研究所
Materials & Advanced Research Laboratory
Research & Development Division

増野敦信　Atsunobu MASUNO
弘前大学
Hirosaki University

佐藤　至　Itaru SATO
研究開発本部　材料・要素技術研究所
Materials & Advanced Research Laboratory
Research & Development Division

江面嘉信　Yoshinobu EZURA
研究開発本部　材料・要素技術研究所
Materials & Advanced Research Laboratory
Research & Development Division

井上博之　Hiroyuki INOUE
東京大学
The University of Tokyo

上田　基　Motoi UEDA
研究開発本部　材料・要素技術研究所
Materials & Advanced Research Laboratory
Research & Development Division

水口雅史　Masafumi MIZUGUCHI
研究開発本部　材料・要素技術研究所
Materials & Advanced Research Laboratory
Research & Development Division

山本優也　Yuya YAMAMOTO
研究開発本部　材料・要素技術研究所
Materials & Advanced Research Laboratory
Research & Development Division

吉本幸平
Kohei YOSHIMOTO

増野敦信
Atsunobu MASUNO

佐藤　至
Itaru SATO

江面嘉信
Yoshinobu EZURA

井上博之
Hiroyuki INOUE

上田　基
Motoi UEDA

水口雅史
Masafumi MIZUGUCHI

山本優也
Yuya YAMAMOTO